BOTTOM-DISCONTINUOUS RIEMANN SOLVER FOR MODELING OF WAVE OVERTOPPING

A THESIS SUBMITTED TO THE GRADUATE DIVISION OF THE UNIVERSITY OF HAWAI'I AT MĀNOA IN PARTIAL FULFILLMENT OF THE REQUIREMENTS FOR THE DEGREE OF

MASTER OF SCIENCE

IN

OCEAN AND RESOURCES ENGINEERING

AUGUST 2015

By

Matthew J. Wesley

Thesis Committee:

Kwok Fai Cheung, Chairperson
Zhenhua Huang
Marcelo H. Kobayashi

Acknowledgements

I would like express my gratitude to my advisor, Prof. Cheung, for his guidance and knowledge throughout my graduate studies as well as the rest of my thesis committee. I would like to thank Prof. Oceana Francis for the use of the hydraulics laboratory, Betsy Seiffert for teaching me proper laboratory techniques, the CEE lab technicians, Kim Hartzog and Mitch Pinkerton, for their help with the experimental setup and laboratory facilities, and Troy Heitmann for the informative discussions we had when problems arose. Finally, I would like to thank my family and friends for their inspiration and encouragement throughout my entire education.

This study was supported by the Office of Naval Research under Grant No. N00014-12-1-0721 through an internship in the final semester of my undergraduate program and a research assistantship during my graduate studies.

Abstract

Depth-integrated numerical models represent an adequate and efficient method to describe near-shore processes including wave breaking. A limitation to these models is encountered as a wave overtops a vertical breakwater. The vertical flow structure cannot be recreated, leading to inaccurate results or numerical instabilities. The Riemann solver containing a bottom discontinuity presented by Murillo and Garcia-Navarro (2010; 2012, Journal of Computational Physics) may alleviate this limitation. In this study, a review of the Riemann solver and its incorporation into a one-dimensional second-order MUSCL-Hancock scheme are presented. The first series of validation tests mimics the Riemann problem with an emphasis on overtopping over a bottom discontinuity. The model results give good overall agreement to those from OpenFOAM (an open-source computational fluid dynamics code), but show underestimation of the downstream propagation speed when free fall of water is involved. A laboratory experiment was conducted in a 9.14 m long flume to provide validation data for solitary wave overtopping of a vertical breakwater. The numerical model shows slightly more reflection from the breakwater and underestimates the overtopping volume. Despite the discrepancies, the bottom-discontinuous Riemann solver performs reasonably well in approximating the overall processes given the simplicity of its formulation.

Table of Contents

List of Figures

List of Tables

List of Symbols

C_t: Courant number

$\mathbf{F}$: vector of flux variables

g: acceleration due to gravity

h: water depth

h_0: initial water depth

$\mathbf{J}$: Jacobian matrix

n: Manning factor

p: pressure

s: wave speed

$\mathbf{S}$: vector of source terms

$\bar{\mathbf{S}}$: bottom discontinuity source term

T: thrust term

u: horizontal velocity

$\mathbf{U}$: vector of conserved quantities

$\mathbf{x}$: position vector

η: bed elevation

$\Delta\eta$: bottom discontinuity height

ρ: density

τ_b: bottom shear stress

ζ: surface elevation

1. Introduction

The capability to model overtopping of coastal structures by tsunamis is important. Once overtopping occurs, the flow may cause devastation to population and infrastructure. Modeling of overtopping, especially in the case of a vertical breakwater or seawall, is mathematically challenging, but can be accomplished by three-dimensional computational fluid dynamics models such as Open Field Operation And Manipulation or OpenFOAM (Weller et al., 1998). The computation takes significant resources because of the flow complexities involving vortex formation and air-water interactions and is typically utilized in load and scour prediction (Bricker et al., 2013; Yim et al., 2014). Depth-integrated models based on the nonlinear shallow-water or Boussinesq equations allow simulations of transoceanic tsunami propagation and impact to coastal regions. Implementation of shock-capturing schemes allows approximations of flow discontinuities associated with bore formation and overtopping of vertical walls.

Shock-capturing schemes have been used in depth-integrated equations for modeling of breaking waves as hydraulic jumps, or bores in coastal environments. These shock waves come naturally from the solution to the Riemann problem, which involves two distinct initial states separated by a discontinuity. Godunov (1959) was the first to propose discretization of a conservative system by a series of control volumes and solving a local Riemann problem at each interface to capture flow discontinuities. Roe (1981) provided a local linearization of the problem, which leads to an efficient and accurate approximation of the solution. These earlier works focus on dynamics of ideal gases that follow Euler's equations. Glaister (1988) and Toro (1992) subsequently implemented the shock-capturing scheme to the nonlinear shallow-water equations for bore approximation and obtained the solution to the exact Riemann problem using iterative approaches. Building on these techniques, Hu et al. (2000) investigated the overtopping rate on a parapet wall over a coastal structure by assuming a slope on the face and an open boundary condition for the outgoing flow.

The aforementioned schemes cater to surface and momentum discontinuities. Zhou et al. (2000, 2001) introduced the surface gradient method to eliminate depth-extrapolation errors and subsequently extended the method to include effects of a bottom discontinuity. The energy loss over a bottom discontinuity is approximated by an empirical method and included in the source term of the nonlinear shallow-water equations. Zhou et al. used a traditional Riemann problem that is solved independent of the source term. George (2008) included a bottom discontinuity into the Riemann problem and provided an approximate solver to the augmented system, which ensures momentum conservation of flow over irregular bathymetry. Bernetti et al. (2008) approximated the pressure on a bottom discontinuity as hydrostatic and provided an exact solution to the augmented Riemann problem. Although exact, this solution is not unique and the actual solution to the problem must be determined using other factors such as energy principles and physical constraints. Murillo and Garcia-Navarro (2010, 2012) provided an approximate solution to the Riemann problem but with a source term included in the formulation. A similar source term to Bernetti et al. (2008) can be applied to describe flows over a bottom discontinuity.

The previous studies of bottom-discontinuous Riemann solvers focus on submerged bathymetric features and their capabilities in describing wave overtopping remain an open question. This thesis assesses the implementation of the Riemann solver proposed by Murillo and Garcia-Navarro (2012) in a nonlinear shallow-water model to account for overtopping of vertical breakwaters and the resulting flow on the leeside. Their well-balanced scheme provides an accurate estimation of wetting and drying fronts as well as a steady-state preservation even when small perturbations are present in the water surface. Although the Riemann problem does not contain the vertical flow structure to physically describe overtopping, the numerical scheme is efficient and may provide an approximation of the local processes in a regional simulation for flood hazard assessment. A two-fold approach is applied to assess the resulting nonlinear shallow-water model. The model is first applied to the Riemann problem with a bottom

discontinuity and the results are compared with those from OpenFOAM. A laboratory flume experiment involving solitary wave overtopping a vertical breakwater is conducted to provide additional data to assess the validity of the numerical model.

2. Mathematical Formulation

This section focuses on the development of a nonlinear shallow-water model that utilizes the bottom-discontinuous Riemann solver presented by Murillo and Garcia-Navarro (2010, 2012). A brief summary of the Riemann problem is presented and basic aspects are described in relation to a discontinuity in a flow field. The treatment of the bottom discontinuity is summarized and the solver is incorporated into a second-order numerical scheme for the solution of the nonlinear shallow-water equations.

2.1 Governing Equations

A nonlinear shallow-water model is applicable when the flow depth h is small in relation to a characteristic horizontal dimension such as the wavelength L in the case of periodic waves. For tsunamis, the wave period can be upward of 30 minutes, which yields an $h/L << 1/20$ to satisfy the shallow-water condition even in the open ocean. Although dispersion effects may be important during propagation, the flux-dominated waves can reasonably be approximated by the shallow-water equations.

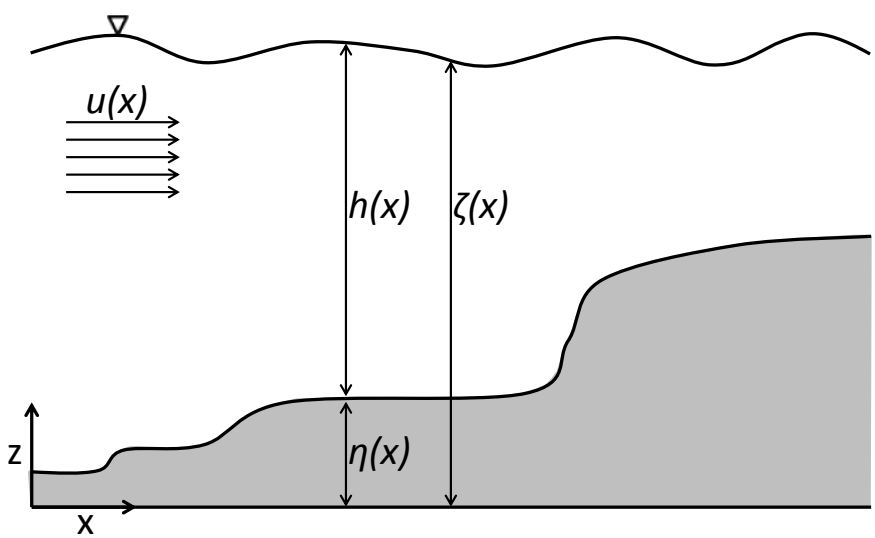

Figure 1: Variable definition for the SWE

To derive the nonlinear shallow-water equations, one must make assumptions to simplify the flow field. These include an incompressible and inviscid fluid and a irrotational flow. Either hydrostatic pressure can be assumed *a priori* leading to negligible vertical accelerations, or the vertical terms can be assumed to be small leading to *a posterior* definition of hydrostatic pressure from a perturbation analysis. Figure 1 provides a definition sketch of the variables in a Cartesian coordinate system (x, z). Written in the conservative form in one dimension, the flow is defined by the continuity and momentum equations as

$$h_t + (hu)_x = 0 \tag{1}$$

$$(hu)_t + \left(hu^2 + \frac{1}{2}gh^2\right)_x = -gh\eta_x - \frac{\tau_b}{\rho} \tag{2}$$

in which the bottom friction τ_b is given in terms of a Manning number n by

$$\tau_b = \rho g \frac{n^2}{h^{1/3}} u|u| \tag{3}$$

where u is the horizontal velocity, g is acceleration due to gravity, η is the bed elevation, ρ is the fluid density, and the subscripts t and x denote differentiation with respect to time and space. The source terms associated with the bed slope and bottom friction, which contribute to the change in momentum, are grouped on the right hand side of the equation.

The governing equations (1) and (2) represent conservation of mass and momentum. Since the source terms are included, the expression of a conservation law should not be used because the flux must be balanced by the source terms. In vector form, this balance law becomes:

$$\mathbf{U}_t + \mathbf{F}(\mathbf{U})_x = \mathbf{S} \tag{4}$$

where **U** is the vector of conserved variables, **F**(**U**) is the flux vector, and **S** contains the source terms defined respectively as

$$\mathbf{U} = \begin{bmatrix} h \\ hu \end{bmatrix} \tag{5}$$

$$\mathbf{F}(\mathbf{U}) = \begin{bmatrix} hu \\ hu^2 + \frac{1}{2}gh^2 \end{bmatrix} \tag{6}$$

$$\mathbf{S} = \begin{bmatrix} 0 \\ -gh\eta_x - \frac{\tau_b}{\rho} \end{bmatrix} \tag{7}$$

If a discontinuity is present, the system requires additional mathematical or numerical treatments to conserve mass and momentum. The nonlinear shallow-water equations in matrix form (4) allow implementation of a Godunov-type scheme, which discretizes the domain into computational cells and utilizes a Riemann solver to impose conservation across flow discontinuities at the cell interface.

2.2 Riemann Problem

The Riemann problem consists of a hyperbolic system with two constant states separated by an initial discontinuity. The formulation typically excludes the bottom slope and friction, which are treated as source terms in a Godunov-type scheme. The solution consists of left and right propagation waves separated by a middle state in the so-called star region. In the exact solution, the middle state must be solved from the nonlinear shallow-water equations using an iterative scheme such as the Newton-Raphson method. Roe (1981) proposed an approximate solution that involves linearization of the homogeneous governing equations as

$$\mathbf{U}_t + \mathbf{F}'(\mathbf{U})\mathbf{U}_x = \mathbf{0} \tag{8}$$

in which **F**'(**U**) is the Jacobian matrix given by:

$$\mathbf{F}'(\mathbf{U}) = \mathbf{J} = \begin{bmatrix} 0 & 1 \\ -u^2 + gh & 2u \end{bmatrix} \tag{9}$$

where *h* is a constant depth. The matrix has two eigenvalues:

$$\lambda_1 = u - \sqrt{gh} \tag{10}$$

$$\lambda_2 = u + \sqrt{gh} \tag{11}$$

which represent the propagation speeds on the two sides of the initial discontinuity. Since the Jacobian is diagonalizable, the system (8) is hyperbolic as in the case of the homogenous shallow-water equations and therefore can be applied to define the Riemann problem. Since the constant Jacobian is developed to connect the two states, the variables assume average values from the two sides in the form

$$\tilde{u} = \frac{u_L\sqrt{h_L} + u_R\sqrt{h_R}}{\sqrt{h_L} + \sqrt{h_R}} \tag{12}$$

$$\tilde{h} = \frac{h_L + h_R}{2} \tag{13}$$

where the subscripts L and R denote variables on the left and right sides. Implementation of these so-called Roe averages in (12) and (13) lead to estimates of the eigenvalues $\tilde{\lambda}_1$ and $\tilde{\lambda}_2$.

The implementation of Riemann solvers based on homogeneous governing equations requires treatment of the bottom slope as a source term in a Godunov-type scheme. The bottom discontinuity can be considered a limiting condition as the bed slope approaches infinity

$$\frac{\partial \eta}{\partial x} \to \infty \tag{14}$$

If left untreated in the Godunov-type scheme, unrealistic velocities would appear near the bottom discontinuity. Numerical models typically require smoothing of the bathymetry to limit the bed slope within an acceptable range, but this is not always viable as in the case of a vertical breakwater. As a more general approach, the source term associated with the bottom discontinuity can be reformulated and included in the Riemann problem. Figure 2 shows the initial conditions of the Riemann problem with a left and right state separated by a discontinuity in the water surface and bottom elevation.

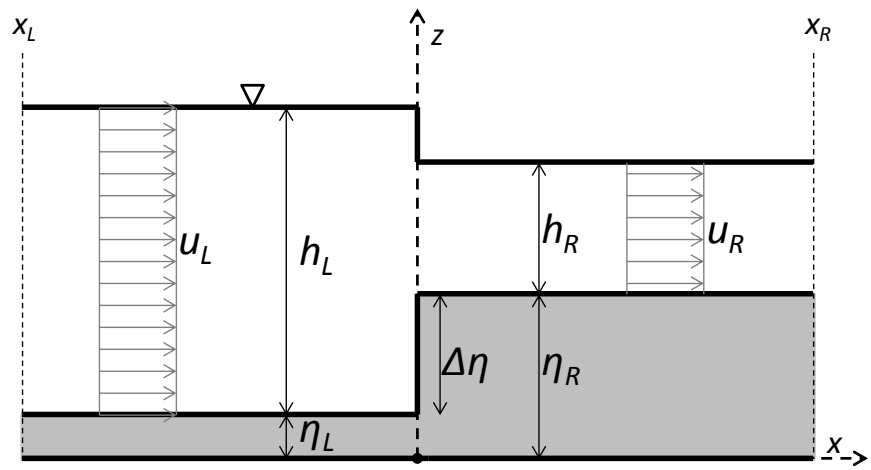

Figure 2: Initial conditions for Riemann problem

The solution to the Riemann problem with the source term included, proposed by Murillo and Garcia-Navarro (2010; 2012), begins with the weak form of the nonlinear shallow-water equations:

$$\int_0^T \int_{-\infty}^{\infty} (\mathbf{U}_t + \mathbf{F}(\mathbf{U})_x - \mathbf{S}) dx\, dt = \mathbf{0} \tag{15}$$

The weak form allows for discontinuities in the vector of conserved quantities and when applied to the Riemann problem, yields the approximation

$$\int_0^{\Delta t} \int_{x_L}^{x_R} (\mathbf{U}_t + \mathbf{F}(\mathbf{U})_x - \mathbf{S}) dx\, dt = \mathbf{0} \tag{16}$$

where Δt is a small time interval. Solving for the vector of conserved variables gives:

$$\int_{x_L}^{x_R} \mathbf{U}(x, \Delta t) dx = x_R \mathbf{U}_R - x_L \mathbf{U}_L - (\mathbf{F}_R - \mathbf{F}_L - \bar{\mathbf{S}})\Delta t \tag{17}$$

where $\bar{\mathbf{S}}$ an average source term over the integrated area and is assumed to be linear in time. The distance traveled is directly dependent on the characteristic speeds s_L and s_R,

$$x_L \leq s_L \Delta t \quad \& \quad x_R \geq s_R \Delta t \tag{18}$$

The integral average of the vector of conserved variables is defined as

$$\bar{\mathbf{U}} = \frac{\int_{x_L}^{x_R} \mathbf{U}(x, \Delta t) dx}{\Delta t (s_R - s_L)} \tag{19}$$

which leads to the solution for the middle state or the star region

$$\bar{\mathbf{U}}^* = \frac{s_R \mathbf{U}_R - s_L \mathbf{U}_L - \mathbf{F}_R + \mathbf{F}_L + \bar{\mathbf{S}}}{(s_R - s_L)} \tag{20}$$

If no source term is present ($\bar{\mathbf{S}} = 0$), this corresponds to the solution given by Toro (1992) for the HLL solver with a flat bed.

Since the source term is not zero, the Jacobian has a third eigenvalue, which corresponds to a stationary jump at the bottom discontinuity. The middle state has two distinct solutions on the left and right sides

$$\mathbf{U}_L^* = \frac{\int_{x_L}^{0} \mathbf{U}(x, \Delta t) dx}{-\Delta t s_L} \tag{21}$$

$$\mathbf{U}_R^* = \frac{\int_{0}^{x_R} \mathbf{U}(x, \Delta t) dx}{\Delta t s_R} \tag{22}$$

which are directly determined from the conserved quantities within that middle state. The energy across a shock wave must follow the Rankine-Hugoniot jump condition, which must be true for the two middle states and across the bottom discontinuity

$$\mathbf{F}_L^* - \mathbf{F}_L = s_L (\mathbf{U}_L^* - \mathbf{U}_L) \tag{23}$$

$$\mathbf{F}_R - \mathbf{F}_R^* = s_R (\mathbf{U}_R - \mathbf{U}_R^*) \tag{24}$$

$$\mathbf{F}_R^* - \mathbf{F}_L^* - \bar{\mathbf{S}} = S_m (\mathbf{U}_R^* - \mathbf{U}_L^*) \tag{25}$$

The characteristic speed is zero ($S_m = 0$) for the stationary jump at the bottom discontinuity. Therefore, equation (25) becomes

$$\mathbf{F}_R^* - \mathbf{F}_L^* = \bar{\mathbf{S}} \tag{26}$$

which provides a relationship between the two middle fluxes. If only shock waves are involved, the middle-state flux difference can be determined from linearization of the homogeneous governing equations to give

$$\mathbf{F}_R^* - \mathbf{F}_L^* = \mathbf{J}\left(\widetilde{\mathbf{U}}^*\right)(\mathbf{U}_R^* - \mathbf{U}_L^*) \tag{27}$$

where $\mathbf{J}$ denote the Jacobian and $\widetilde{\mathbf{U}}$ is a Roe (1981) average. Since the star region is unknown *a priori*, the Jacobian is approximated with the initial state as

$$\mathbf{J}\left(\widetilde{\mathbf{U}}^*\right) \approx \mathbf{J}(\widetilde{\mathbf{U}}) \tag{28}$$

Substituting equation (27) into (26) yields:

$$\mathbf{J}(\widetilde{\mathbf{U}})(\mathbf{U}_R^* - \mathbf{U}_L^*) = \bar{\mathbf{S}} \tag{29}$$

Solving the simultaneous equations (23), (24), (26), and (29) gives an explicit definition of the middle states in terms of the vector of conserved variables

$$\mathbf{U}_L^* = \frac{s_R\mathbf{U}_R - s_L\mathbf{U}_L + \mathbf{F}_L - \mathbf{F}_R + \bar{\mathbf{S}} - s_L\bar{\mathbf{H}}}{s_R - s_L} \tag{30}$$

$$\mathbf{U}_R^* = \frac{s_R\mathbf{U}_R - s_L\mathbf{U}_L + \mathbf{F}_L - \mathbf{F}_R + \bar{\mathbf{S}} - s_R\bar{\mathbf{H}}}{s_R - s_L} \tag{31}$$

$$\mathbf{F}_R^* = \frac{s_R\mathbf{F}_L - s_L\mathbf{F}_R + s_L s_R(\mathbf{U}_R - \mathbf{U}_L) + s_R(\bar{\mathbf{S}} - s_L\bar{\mathbf{H}})}{s_R - s_L} \tag{32}$$

$$\mathbf{F}_L^* = \frac{s_R\mathbf{F}_L - s_L\mathbf{F}_R + s_L s_R(\mathbf{U}_R - \mathbf{U}_L) + s_L(\bar{\mathbf{S}} - s_R\bar{\mathbf{H}})}{s_R - s_L} \tag{33}$$

where

$$\bar{\mathbf{H}} = \bar{\mathbf{S}}\,\mathbf{J}^{-1} \tag{34}$$

that can be incorporated into a Godunov-type scheme.

This solution to the Riemann problem, along with the standard solution without considering the source terms, consists of waves that propagate away from the initial discontinuity

in the form of a shock or rarefaction. A shock wave is a discontinuity that propagates at a characteristic speed s_L or s_R according to the Rankine-Hugonoit conditions. A rarefaction wave is a smooth transition from one state to another that travels with a speed given by the Riemann invariants as:

$$u - 2\sqrt{gh} = r = constant \tag{35}$$

$$u + 2\sqrt{gh} = s = constant \tag{36}$$

Figure 3 presents a visual solution to the Riemann problem. The rarefaction and shock waves travel away from a stationary shock located at the bottom discontinuity. The figure shows both the spatial and time evolution. The spatial evolution at the bottom shows the initial conditions as a dashed line and the solution to the Riemann problem after an elapsed time. The upper part shows the positions of the traveling and stationary waves over time.

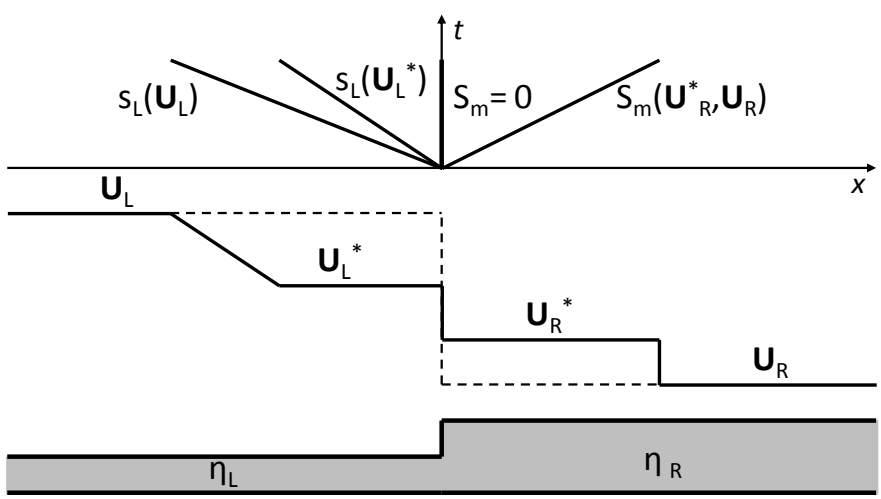

Figure 3: Solution to the Riemann problem with a bottom discontinuity evolved in space (bottom) and time (top)

The solution to the Riemann problem includes a source term, which balances the momentum across the bottom discontinuity. As the bottom slope becomes infinite at the discontinuity, George (2008) defined the source term as

$$gh\eta_x \rightarrow g\tilde{h}\Delta\eta\delta(x) \tag{37}$$

where $\Delta\eta = \eta_R - \eta_L$ is the step height and $\delta(x)$ is a delta function. This definition is adequate when considering submerged bottom discontinuities, but as $\Delta\eta$ becomes larger than the average water depth, this approach overestimates the influence of the bottom step. An alternative is to impose a hydrostatic pressure distribution on the discontinuity as a source term (Bernetti et al., 2009; Murillo and Garcia-Navarro, 2012). Figure 4 provides an illustration of the force balance across the bottom discontinuity. The hydrostatic pressure on the step contributes to a thrust term in relation to the flow direction

$$T = \rho g\left(h_j - \frac{|\Delta\eta'|}{2}\right)\Delta\eta' \tag{38}$$

in which

$$h_j = \begin{cases} h_L & if\ \Delta\eta \geq 0 \\ h_R & if\ \Delta\eta < 0 \end{cases} \tag{39}$$

$$\Delta\eta' = \begin{cases} h_L & if\ \Delta\eta \geq 0\ \&\ \zeta_L < \eta_R \\ h_R & if\ \Delta\eta < 0\ \&\ \zeta_R < \eta_L \\ \Delta\eta & otherwise \end{cases} \tag{40}$$

The hydrostatic pressure distribution is literally determined by the flow depth facing the step and is consistent with the shallow-water assumption. Combining the two approaches, Murillo and Garcia-Navarro (2012) proposed the use of equation (37) when both sides are submerged and (38) when either side is dry, giving rise to

$$T_{max} = \begin{cases} \max\left(\rho g\tilde{h}\Delta\eta\ , T\right) & if\ \Delta\zeta\Delta\eta \geq 0\ and\ \tilde{u}\Delta\eta > 0 \\ T & otherwise \end{cases} \tag{41}$$

with $\Delta\zeta = \zeta_R - \zeta_L$. The source term due to the bottom discontinuity is defined as $\bar{\mathbf{S}} = [0, -T_{max}/\rho]^T$

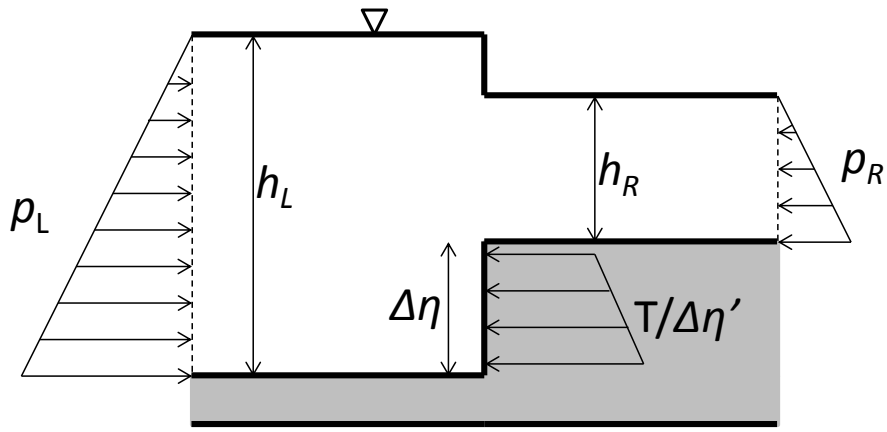

Figure 4: Definition of thrust source term based on initial conditions

2.3 Numerical Scheme

A modified HLL (Harten, van Leer and Lax) Godunov-type scheme is used to solve the governing equation (4) for practical application. This includes discretization of the domain into a series of cells and implementation of a local Riemann solver at each interface. The grid set-up consists of cell centered values at *i* and interface values at *i*±½. Variables can be defined as piece-wise constant or piece-wise linear in each cell as shown Figure 5. As with any Godunov-type scheme, the Riemann problem must be solved at each cell interface to determine the flux into and out of the cell. The modified HLL scheme, also known as the HLLS (S for step), can uniquely define the middle-state water depths and velocities on the two sides of a bottom discontinuity (Murillo and Garcia-Navarro, 2012). A second-order upwind MUSCL-Hancock scheme consisting of both a predictor and a corrector step evolves the conserved variables in time

$$\mathbf{U}_i^{n+\frac{1}{2}} = \mathbf{U}_i^n - \frac{\Delta t}{2\,\Delta x}\left[\left((\mathbf{F}_L)^n_{i+\frac{1}{2}} - (\mathbf{F}_R)^n_{i-\frac{1}{2}}\right) - \mathbf{S}_i^n\right] \tag{42}$$

$$\mathbf{U}_i^{n+1} = \mathbf{U}_i^n - \frac{\Delta t}{\Delta x}\left[\left(\left(\mathbf{F}^-_{i+\frac{1}{2}}\right)^{n+\frac{1}{2}} - \left(\mathbf{F}^+_{i-\frac{1}{2}}\right)^{n+\frac{1}{2}}\right) - \mathbf{S}_i^{n+\frac{1}{2}}\right] \tag{43}$$

where Δx and Δt denote the cell and time step sizes and n is the current time step. With the bottom discontinuity incorporated in the Riemann solver, the source terms include the bottom slope and friction as defined in equation (7). In the predictor step (42), the conserved variables are evolved over a half time step based on the flux and source terms at the current time. The conserved variables determined at the predictor step define the Riemann solution on the left and right sides of the interface, denoted by minus and plus signs in the superscripts of equation (50). Together with the source term, these variables update the flow over a full time step.

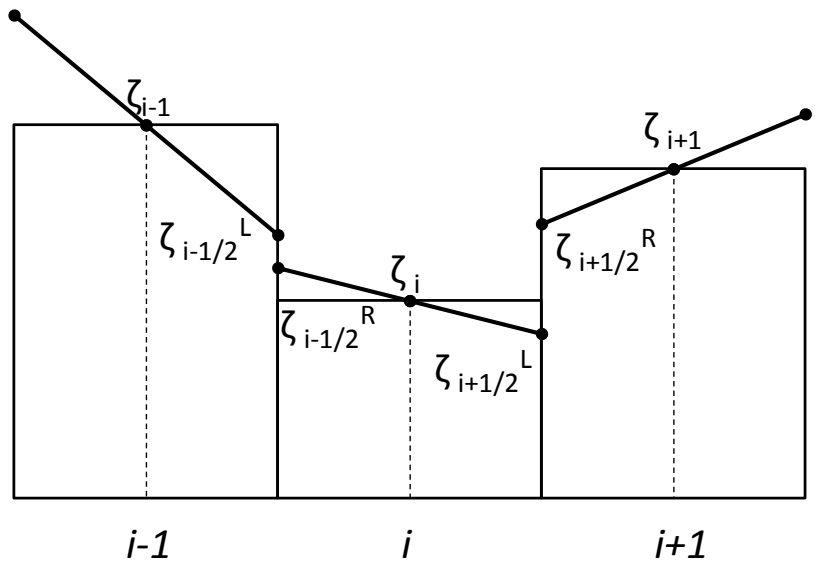

Figure 5: Piece-wise linear data reconstruction

Both the predictor and corrector steps involve reconstruction of the interface fluxes from the conserved variables at the cell centers using a second-order scheme. The surface gradient method proposed by Zhou et. al. (2001) reconstructs the interface surface elevations instead of the flow depth to eliminate depth-interpolation errors. To reduce spurious oscillations, a slope limiter is applied during variable reconstruction for the piece-wise linear distribution. In this study, the superbee limiter is used as it allows a greater steepness for shock capturing in comparison to other approaches such as minmod and van Leer. The limiter is applied to both the

surface elevation and momentum before the computation of the interface fluxes. Near the bottom discontinuity, a second-order limiter provides unrealistic reconstruction values. A first-order limiter with upwind or downwind bias is applied within the cells adjacent to the discontinuity. The first-order limiter only uses information from the respective side so as not to create an artificial slope across the bottom discontinuity, which is important when considering a bottom discontinuity that is greater than the water depth.

The corrector step invokes the Riemann solver to ensure conservation across discontinuities. The explicit definition of the middle state by equations (32) and (33) provides the fluxes into and out of the cell. Since the flow cannot transition from sub- to super-critical within the cell or vice versa, the interface fluxes on the two sides are:

$$\mathbf{F}^{-}_{i+\frac{1}{2}} = \begin{cases} \mathbf{F}_L & if\ 0 \leq s_L \\ \dfrac{s_R\mathbf{F}_L - s_L\mathbf{F}_R + s_L s_R(\mathbf{U}_R - \mathbf{U}_L) + s_L\left(\bar{\mathbf{S}}_{i+\frac{1}{2}} - s_R\bar{\mathbf{H}}_{i+\frac{1}{2}}\right)}{s_R - s_L} & if\ s_L \leq 0 \leq s_R \\ \mathbf{F}_R - \bar{\mathbf{S}}_{i+\frac{1}{2}} & if\ 0 \geq s_R \end{cases} \tag{44}$$

$$\mathbf{F}^{+}_{i+\frac{1}{2}} = \begin{cases} \mathbf{F}_L + \bar{\mathbf{S}}_{i+\frac{1}{2}} & if\ 0 \leq s_L \\ \dfrac{s_R\mathbf{F}_L - s_L\mathbf{F}_R + s_L s_R(\mathbf{U}_R - \mathbf{U}_L) + s_R\left(\bar{\mathbf{S}}_{i+\frac{1}{2}} - s_L\bar{\mathbf{H}}_{i+\frac{1}{2}}\right)}{s_R - s_L} & if\ s_L \leq 0 \leq s_R \\ \mathbf{F}_R & if\ 0 \geq s_R \end{cases} \tag{45}$$

Equations (44) and (45) are also known as the HLLS solver. In the presence of a bottom discontinuity, the Jacobian of the middle state is approximated by the initial conditions leading to the definition of $\bar{\boldsymbol{H}}$. The Roe-averaged wave speeds are used instead of those recommended by Einfeldt (1988) and Toro (1992) to balance this term. This gives rise to the wave speeds

$$s_L = \begin{cases} \min\left(u_L - \sqrt{gh_L}\,, u^* - \sqrt{\phi^*}, \tilde{u} - \sqrt{g\tilde{h}}\right) & if\ \bar{\mathbf{S}} = 0 \\ \tilde{u} - \sqrt{g\tilde{h}} & if\ \bar{\mathbf{S}} \neq 0 \end{cases} \tag{46}$$

$$s_R = \begin{cases} \max\left(u_R + \sqrt{gh_R}\,, u^* + \sqrt{\phi^*}\,, \tilde{u} + \sqrt{g\tilde{h}}\right) & if\ \bar{\mathbf{S}} = 0 \\ \tilde{u} + \sqrt{g\tilde{h}} & if\ \bar{\mathbf{S}} \neq 0 \end{cases} \tag{47}$$

in which

$$u^* = \frac{u_L + u_R}{2} + \sqrt{gh_L} - \sqrt{gh_R} \tag{48}$$

$$\sqrt{\phi^*} = \frac{\sqrt{gh_L} + \sqrt{gh_R}}{2} + \frac{u_L - u_R}{4} \tag{49}$$

If a dry cell is adjacent to a wet cell, the wave speeds are modified according to Hu et al. (2000):

$$s_L = u_L - \sqrt{gh_L} \quad s_R = u_L + 2\sqrt{gh_L} \tag{50}$$

$$s_L = u_R - 2\sqrt{gh_R} \quad s_R = u_R + \sqrt{gh_R} \tag{51}$$

for a dry bed to the right and left except if adjacent to bottom discontinuity where the Roe-averaged wave speeds must be used.

Open or reflective conditions can be applied along the boundaries of the computational domain. The boundary conditions for the MUSCL-Hancock scheme consist of ghost cells outside the domain. An open boundary condition allows for flow to exit the domain without producing a reflection that interferes with the solution. In the present one-dimensional formulation with *M* cells, the ghost cells (*M*+1) and (*M*+2) at the downstream end are defined as:

$$h_{M+1} = h_M\,, u_{M+1} = u_M \tag{52}$$

$$h_{M+2} = h_{M-1}\,, u_{M+2} = u_{M-1} \tag{53}$$

and for a reflective boundary,

$$h_{M+1} = h_M \, , u_{M+1} = -u_M \tag{54}$$

$$h_{M+2} = h_{M-1} \, , u_{M+2} = -u_{M-1} \tag{55}$$

These boundary conditions work well in one and two dimensions and maintain second-order accuracy. The time step size is directly related to the wave speed estimation and computational cell size. As in any numerical method, the Courant-Friedrichs-Lewy (CFL) condition determines the time step size as:

$$\Delta t = C_t \min\left(\frac{\Delta x_i}{u_i + \sqrt{g h_i}}\right) \tag{56}$$

where C_t is the Courant number of less than one to ensure stability of the scheme. For this study, the Courant number is 0.5.

3. Verification with CFD Model

For this study, the Riemann problem is based on the nonlinear shallow-water equation without considering the flow in the vertical direction. This becomes a challenge when the bottom step is large or when overtopping is considered. The effects are represented by a source term, which is represented as a horizontal force, in the governing equations. The numerical solution is first examined by a series of simple test cases which illustrate and verify the basic features of the Riemann solver. The results are compared with the solution found by OpenFOAM, an open source computational fluid dynamics (CFD) code. Since OpenFOAM fully accounts for the vertical flow structure and includes air-water interactions, it can provide a baseline for comparison.

The InterFOAM solver within OpenFOAM makes use of the volume of fluid (VoF) technique to track the air-water interface. The VoF technique uses a scalar function α, which evolves in space and time in response to the amount of water in each computational cell. When the cell is completely filled by water, α=1 and when filled with air, α=0. If a mixture of water and air is present in the cell, the value of α defines the ratio of air to water; typically a value of 0.5 defines the air-water interface. The InterFOAM solver is based on the Navier-Stokes equations for each phase simultaneously. For this application, the Euler equations in two dimensions are utilized for the inviscid fluid assumption in the shallow-water equations. The dynamic viscosity in the Navier-Stokes equation is set to zero to obtain Euler's equations

$$\nabla \cdot \mathbf{U} = \mathbf{0} \tag{57}$$

$$\frac{\partial(\rho \mathbf{U})}{\partial t} + \nabla \cdot (\rho \mathbf{U}\mathbf{U}) = -\nabla p - \mathbf{g}\mathbf{x}\nabla\rho \tag{58}$$

where **U** is now the velocity vector, **g** is a body force vector, **x** is the position vector, and the density ρ is no longer constant as it varies across the water-air interface.

The test cases are devised to mimic the Riemann problem with two initial states separated by a discontinuity as illustrated in Figure 2. The initial discontinuities of the water surface and bottom are at $x = 0$. Table 1 lists the initial conditions of the test cases, each of which examines a certain aspect in the problem. The computational domains correspond to a flume with an air-water interface. The free slip condition and a zero pressure gradient are applied at all boundaries. The initial conditions also define the upstream boundary conditions on the left side and a reflective condition is imposed at the downstream boundary. Sensitivity tests showed grid sizes of 0.05 m for the shallow-water modeling using the HLLS solver and 0.02 m by 0.02 m for OpenFOAM to provide converging numerical results for the test cases.

Case 1 is a standard dam-break problem and case 2 simulates a constant surge against an impermeable wall over a flat bottom. Figure 6 shows the initial surface elevations and the numerical solutions from the shallow-water model and OpenFOAM at $t = 5$ s. In the absence of a bottom discontinuity as in case 1, the surface elevation can be obtained analytically from the HLLS solver to verify the numerical solution. The numerical results show a rarefaction wave propagating to the left and a shock wave to the right. Although the shallow-water model cannot describe the surface oscillations or the entrapped air, seen as solid black in the OpenFOAM results, the computed celerity and the middle water depth follow closely with the more complete solution found by OpenFOAM. For the surge against a vertical step in case 2, overtopping should not occur and implementation of ghost cells behind the wall would produce a correct shallow-water solution. However, the hydrostatic assumption of the source term in the HLLS solver does not take into account the inertia force from the sudden deceleration of the incoming flow on the wall. As pointed out by Murillo and Garcia-Navarro (2012), the shallow-water model cannot balance the flux and produces some initial leakage of water up the step. The comparison of the source term with the integrated pressure from OpenFOAM on the step in Table 2 shows the pressure is nearly hydrostatic by $t = 5$ s. The switch from T to the larger T_{max} after the first

time step reduces the amount of water on the step but does not entirely eliminate it. A reflection is produced against the wall and the propagation speed and depth agree quite well with OpenFOAM even with momentum loss due to leakage across the step.

Cases 3 and 4 consist of a dam break problem over a submerged bottom discontinuity with opposing step directions. Figure 7 shows the initial surface elevations and the results from the shallow-water model and OpenFOAM at t = 5 s. With initial still water conditions, the resulting flow can be reasonably approximated with hydrostatic pressure and subsequently the HLLS solver. The shallow-water model gives good agreement with the propagation speeds of the rarefaction and shock in both cases. The OpenFOAM results show dispersion of the wave propagating onto deeper water. The shallow-water model produces a stationary jump associated with the source term above bottom step, while OpenFOAM develops a near-stationary wave slightly downstream of the bottom step. Since the source term is developed to account for the step up, the middle states from case 3 closely follows the solution from OpenFOAM. As indicated in Table 2, the source term computed from equation (41) gives excellent agreement with the integrated pressure on the step from OpenFOAM for case 3. Nevertheless, both cases show the HLLS solver can handle flows over a submerged step reasonably well.

Cases 5 and 6, as illustrated in Figure 8, involve flows across a step onto an initially dry bed without and with an initial velocity. The shallow-water model produces a stationary jump at the step, while OpenFOAM shows a larger jump shifted slightly downstream. The two models give excellent agreement of the advancing front on the dry bed in both cases. With initial still water conditions in case 5, a rarefaction wave propagates toward the left with noticeable dispersion from OpenFOAM. Since an initial velocity is applied in case 6, a refection from the step in the form of a shock wave propagates to the left with a speed and height that agrees well with OpenFOAM. The source terms slightly underestimate the forces from OpenFOAM due to the inertia forces on the step associated with the higher flow speeds in both cases.

Cases 7 and 8 show free fall of water without and with initial velocity onto calm water, while cases 9 and 10 show the same inflow conditions but with a dry bed on the downstream side. Figure 9 compares the results from the shallow-water model and OpenFOAM for cases 7 and 8. The shallow-water model gives an accurate prediction of the rarefaction and overtopping rate, but underestimates the shock speed on the downstream side. Since the shallow-water model reproduces the bore height reasonable well, the lack of air entrainment might account for the lower shock speed in comparison to the OpenFOAM prediction. When the downstream side is initially dry, a rarefaction wave or surge develops as shown in Figure 10 for cases 9 and 10. The shallow-water model gives a good approximation of the propagation speed likely due to reduced air entrainment in the flow as indicated by OpenFOAM. The source term in these cases provides a proxy to account for conversion of potential to kinetic energy during the free fall of water and does not correspond to the forces acting on the step as shown in Table 2. Although the formulation does not fully account for the physical processes, the HLLS solver provides good agreement with OpenFOAM in modeling free fall of water resulting from overtopping of structures.

The 10 test cases show how the HLLS solver handles the basic flow regimes associated with bottom and surface discontinuities. Table 2 shows the switch between T and T_{max} in equation (41) does produce a closer approximation of the force acting on the step with the exception of case 2, in which a larger source term actually helps alleviate a numerical artifact resulting from the HLLS solver. Some limitations are noticed as velocities increase and the hydrostatic assumption begins to deviate. The HLLS solver cannot describe the mechanics of the water fall, but does account for the change in potential energy that indirectly contributes to the momentum gain on the downstream side. The shallow-water model underestimates the bore speed in these cases but still provides reasonable predictions.

Table 1: Initial conditions of test cases

Case	h_L (m)	h_R (m)	u_L (m/s)	u_R (m/s)	η_L (m)	η_R (m)
1	2	1	0	0	0	0
2	0.5	0	0.5	0	0	1
3	2	1.5	0	0	0	1
4	2	1.5	0	0	1	0
5	2	0	0	0	0	1
6	2	0	1	0	0	1
7	1	0.5	0	0	1	0
8	1	0.5	1	0	1	0
9	1	0	0	0	1	0
10	1	0	1	0	1	0

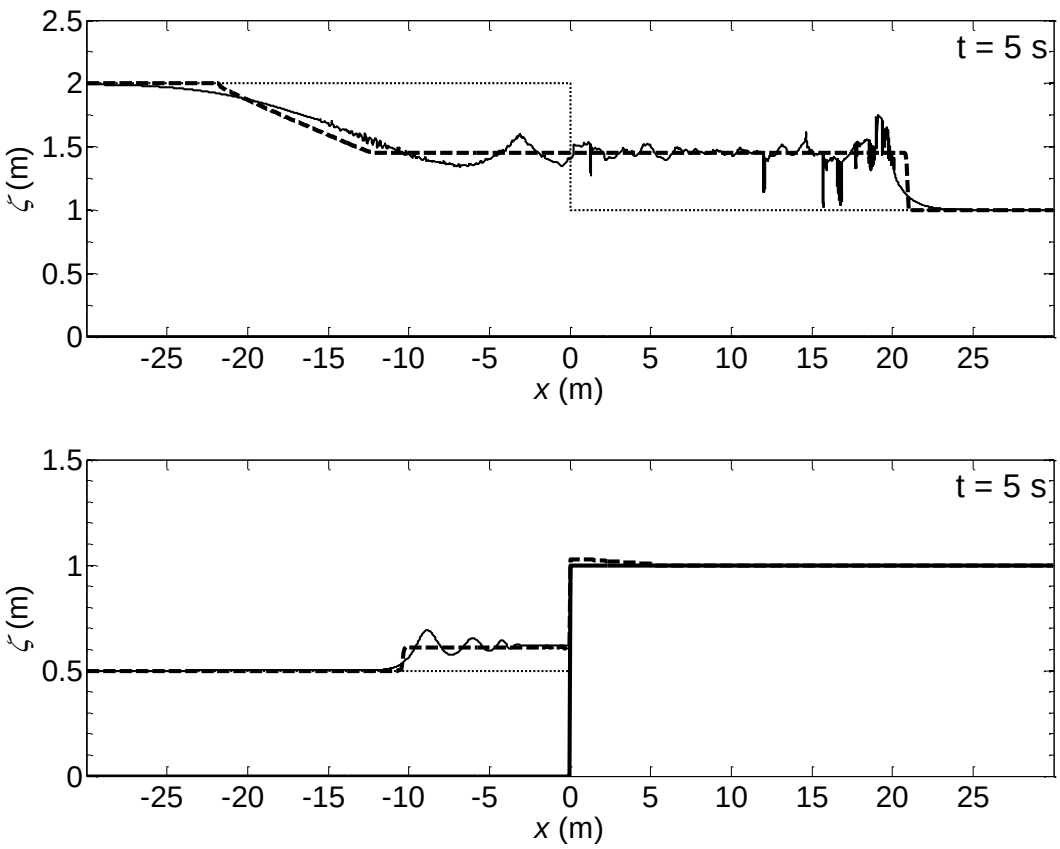

Figure 6: Case 1 (top) and case 2 (bottom) at t = 5 s. HLLS (thick dash) and OpenFOAM (solid) comparison

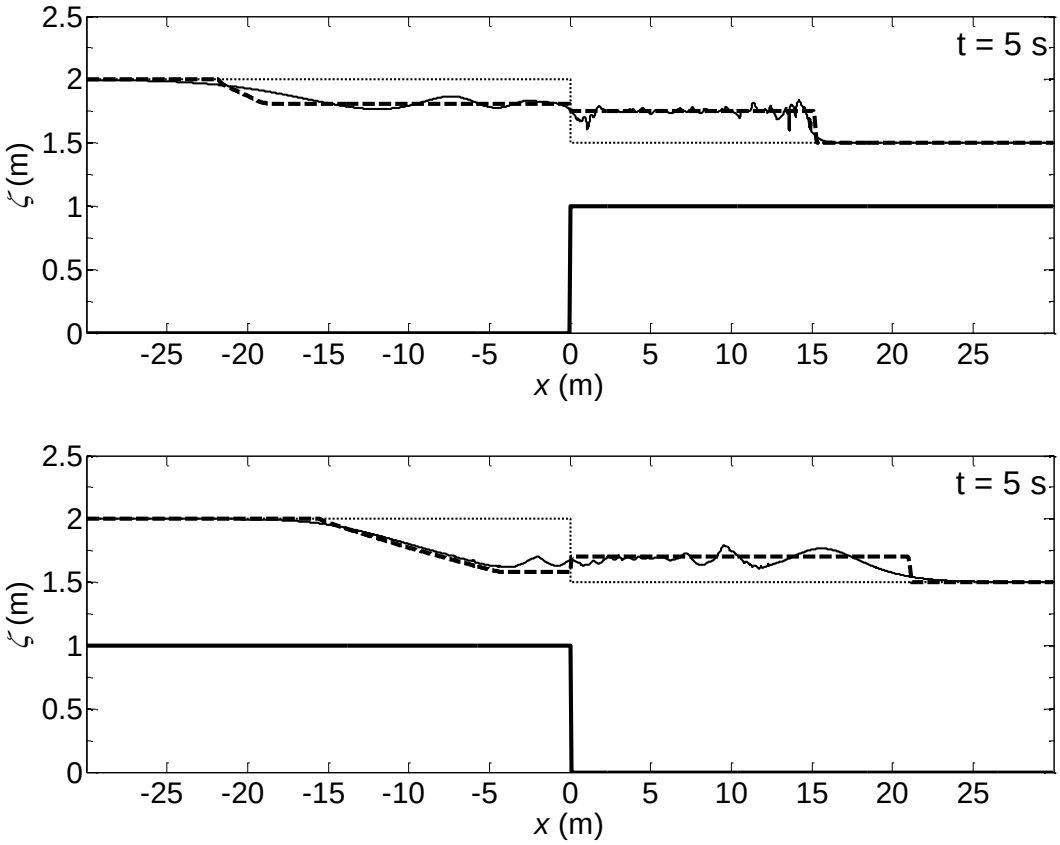

Figure 7: Case 3 (top) and case 4 (bottom) at t = 5 s. Comparison of HLLS solver (thick dash) and OpenFOAM (solid). Bottom elevation shown as thick solid line.

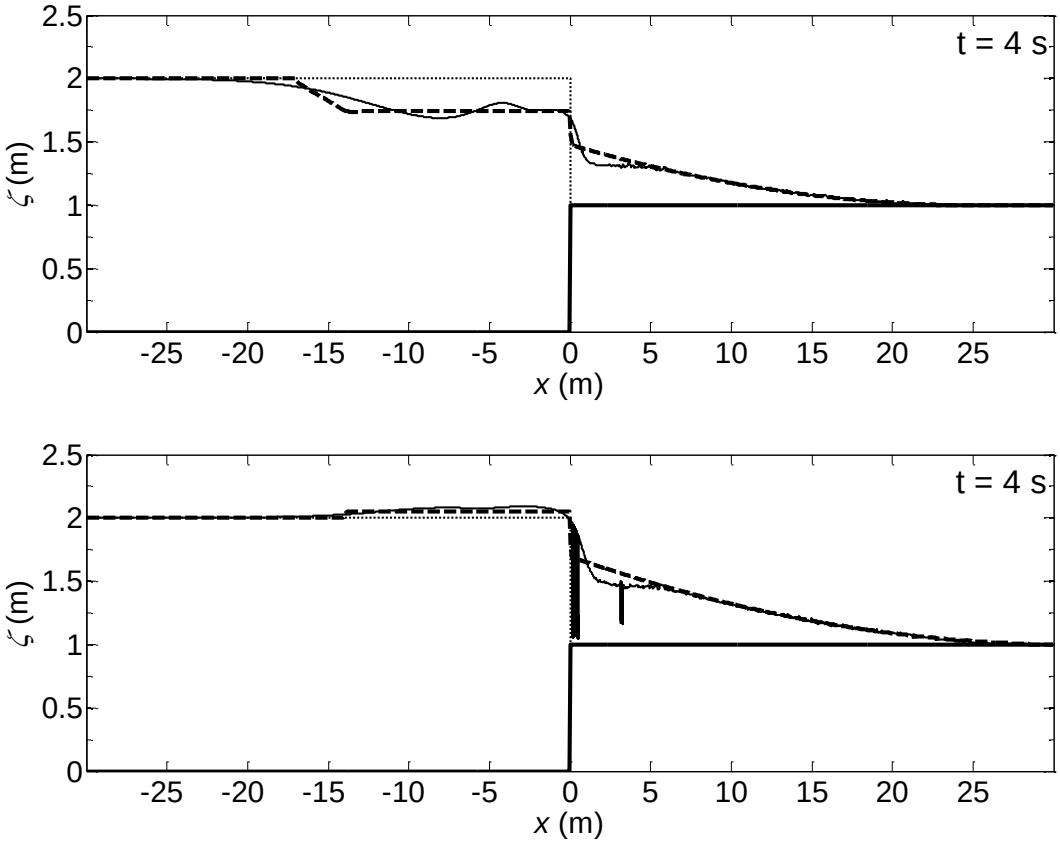

Figure 8: Case 5 (top) and case 6 (bottom) at t = 4 s. HLLS (thick dash) and OpenFOAM (solid) comparison

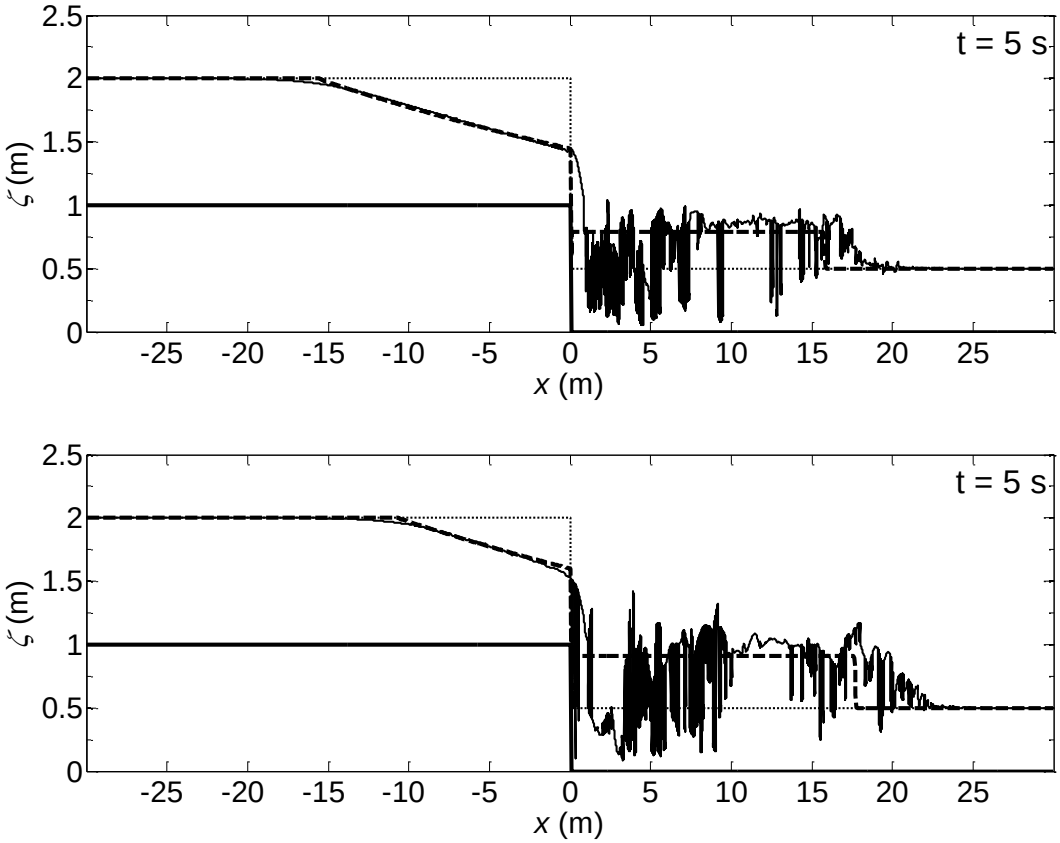

Figure 9: Case 7 (top) and case 8 (bottom) at t = 5 s. HLLS (thick dash) and OpenFOAM (solid) comparison

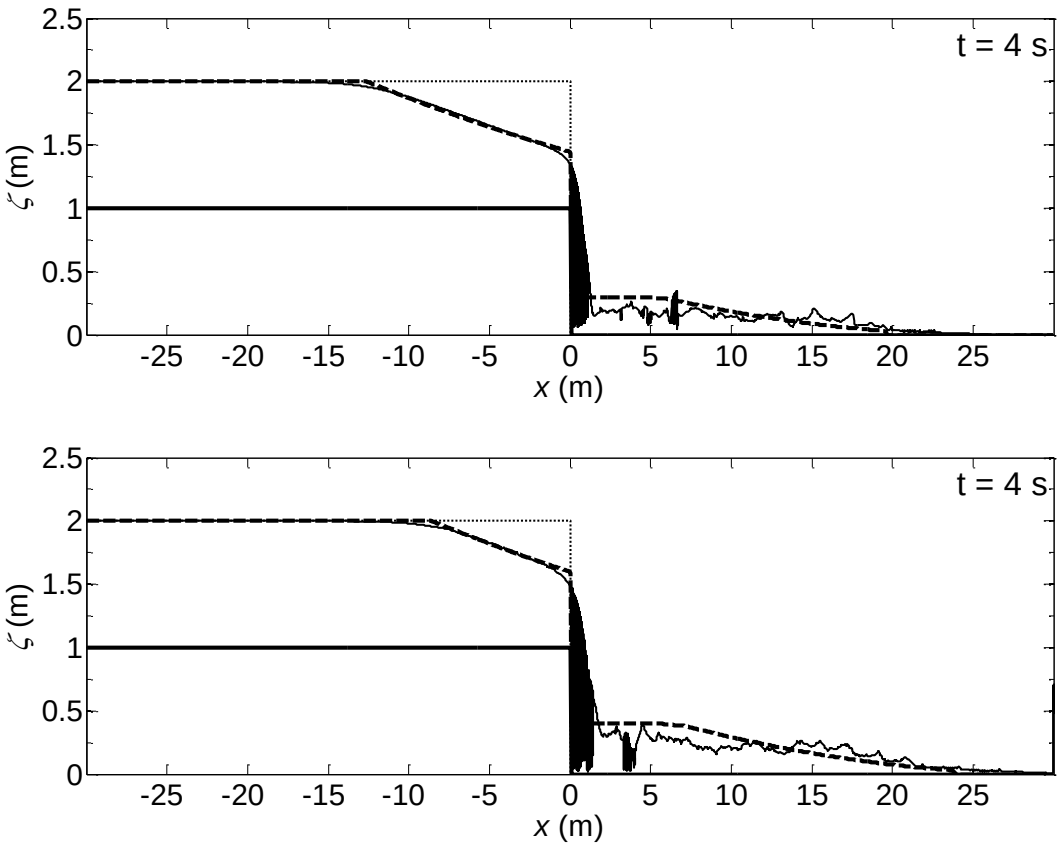

Figure 10: Case 9 (top) and case 10 (bottom) at t = 4 s. Comparison of HLLS solver (thick dash) and OpenFOAM (solid). Bottom elevation shown as thick solid line.

Table 2: Force exerted by bottom step. HLLS solver utilizes underlined values.

Case	F_{OpenFOAM} kN	$F_{\text{hydrostatic}}$ kN	F_{george} kN
2	-1.87	-1.86	<u>-1.90</u>
3	-12.85	<u>-12.85</u>	-12.60
4	-11.29	<u>-10.68</u>	-10.64
5	-12.30	<u>-12.12</u>	-11.25
6	-15.51	<u>-15.12</u>	-13.93
7	1.96	<u>2.82</u>	N/A
8	3.19	<u>3.57</u>	N/A
9	2.10	<u>0.71</u>	N/A
10	2.80	<u>1.20</u>	N/A

4. Validation with Laboratory Experiment

Although there are prior laboratory experiments involving wave overtopping on vertical structures (Franco et al., 1994; Alsop et al., 1995), the published datasets do not include measurements of the reflected and transmitted waves in a form that is suitable for validation of the HLLS solver in the shallow-water model. Therefore, a laboratory experiment was carried out in the Hydraulics Lab of the Department of Civil and Environmental Engineering, University of Hawaii to further investigate the validity of the HLLS solver.

4.1 Laboratory and Numerical Model Setup

The laboratory flume is 9.14 m long, 0.1524 m wide, and 0.39 m high with clear acrylic walls. Figure 11 illustrates the setup of the experiment and instrumentation. The vertical structure is 0.0762 m wide and 0.1524 m tall and made from clear acrylic plastic. This corresponds to a scale of 1:100 for a typical vertical breakwater of 15 m. A piston-type wavemaker generates the incident solitary wave, which provides a series of test cases to illustrate the overtopping and downstream processes and assess the HLLS solver for practical application. The height of the solitary wave is measured from the still-water level and is denoted by a in the figure. Three capacitance-type wave gauges manufactured by JFE Advantech Co., Ltd. sample the surface elevations at 76 Hz with an uncertainty of 5×10^{-5} m. The wave gauges are connected to a data acquisition system controlled by WinLabEM software. A high-speed camera with a Nikkor 50mm f/1.8D lens manufactured by Canadian Photonic Labs Inc. captures the flow across the structure at 400 fps. The camera is placed at 2 m from the face of the wave flume, at an elevation of 0.12192 m from the bottom, and a distance of 0.22 m downstream from the front face of the vertical structure.

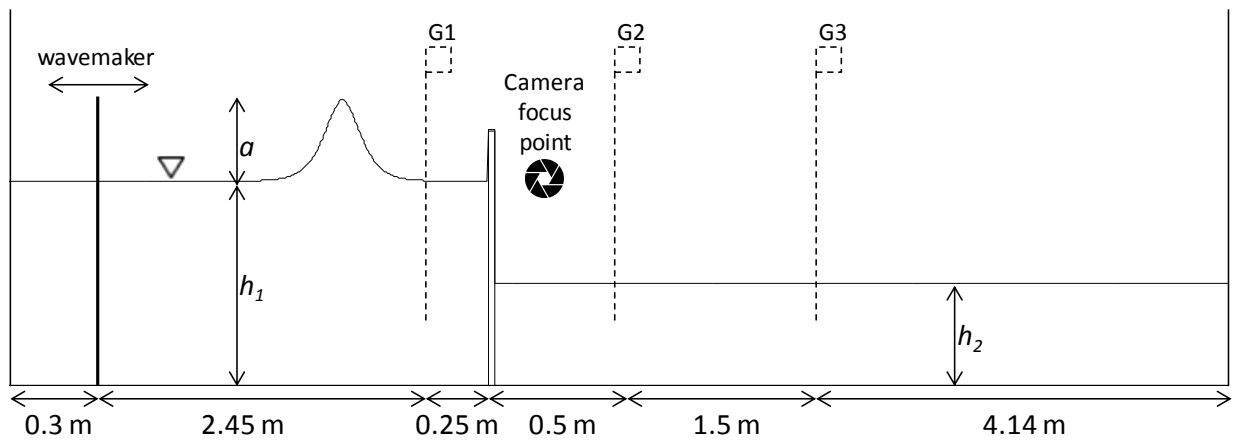

Figure 11: Experimental setup

A total of 30 tests were conducted with a combination of water depths on the two sides of the vertical wall over a range of incident solitary wave conditions. Because of the small-scale experiment, test cases with large relative wave heights a/h_1 produce measurements sufficiently outside instrument uncertainties. Table 3 lists the five selected test cases for illustration of the physical processes and examination of the limitations of the HLLS solver. Tests 1 to 3 examine the effects of the downstream water depth on wave generation and propagation after overtopping. Comparison of the results from tests 2 and 4 illustrates the nonlinear effects, while test 5 provides a more challenging test to examine the capability of the model to handle reflection and overtopping at the same time.

Table 3: Initial conditions for select laboratory trials

Test	h_1 (m)	h_2 (m)	a/h_1
1	0.1524	0.1524	0.3
2	0.1524	0.0762	0.3
3	0.1524	0.0000	0.3
4	0.1524	0.0762	0.2
5	0.1219	0.0610	0.3

The camera recorded the two-dimensional water surface because of the angle of the lens. The surface profile on the front face of the flume is extracted for comparison with the model

results. The post-processing of the high-speed video data includes correction for lens distortion and mapping of pixel coordinates to real-world coordinates. This approach is based on Brady et al. (2004), but without the edge detection techniques. The images are then cropped to compare with the HLLS solver immediately downstream of the structure. The coordinate transformation involves an error of up to 0.026 m. In addition, refraction of light through the side wall of the wave flume causes the image to be slightly offset. This offset of 0.001 m is calculated from Snell's Law using the refractive index of 1.5 for acrylic, a maximum incident angle of 45°, and a 0.0127 wall thickness. The total error for this technique is 0.027 m. The error is greatest near the edges of view and does not have as much of an effect on the image directly in front of the camera.

The shallow-water model covers a flume of 10 m long with the structure located at the center. The incident solitary wave is part of the initial conditions and is positioned such that the surface elevation is less than 1% of the wave height at the front wall of the structure. The grid size on the upstream side needs to have a large value to provide numerical dispersion (Yoon et al., 2007), but is limited to 4.5 cm for resolution of the incident solitary wave. The structure and the downstream side have a much finer grid of 9.5 mm to resolve the more complex flow processes. A Manning number of 0.009 $s/m^{1/3}$ is used to account for the friction on the acrylic surface.

4.2 Results and Discussion

Test 1 has the same water depth on both sides that is equal to the height of the structure. The overtopping does not produce a waterfall and the results provide a baseline for comparison. Figure 12 shows the recorded and computed surface elevation time series at the three gauges. At gauge 1 in front of the structure, the model gives a good depiction of the incident wave but overestimates the reflection from the structure. After gauge 1, the wave transforms into a surge

over the structure. The subsequent gauges recorded a developing wave packet with increasing periods downstream while the model produces a solitary wave with a slightly lower propagation speed. Due to the lack of dispersion, the front face of the solitary wave steepens as it propagates downstream. The computed wave height is comparable to the amplitude of the leading wave in the packet. Figure 13 shows the computed surface elevation with a snapshot from the recorded video. The comparison gives good overall agreement except near the rear of the structure, where the model results show a surface discontinuity as the flow transition from supercritical to subcritical across the step. The abrupt transition at the step results from the source term in the HLLS solver. In reality, the transition occurs over a short distance downstream of the step as shown in the video image.

Test 2 has the same initial condition as 1 in front of the structure, but half of the water depth on the downstream side to produce a waterfall after overtopping. Figure 14 compares the recorded and computed surface elevation time series. The results at gauge 1 are not sensitive to the downstream conditions and are similar to those in test 1. On the downstream side, the model produces a solitary wave with a steepening wave front and decreasing height. Measurements from the gauges show a large leading wave followed by a wave train. The video image in Figure 15 shows a jet from the top of the structure impinging the downstream water surface with significant air entrapment. This jet generates surface waves in opposing directions and the upstream traveling waves reflect against the back face of the structure. The subsequent waves observed at gauges 2 and 3 include reflection from the structure.

Test 3 has a dry bed on the downstream side but the same solitary wave conditions as tests 1 and 2. The results at gauge 1 are similar to those in tests 1 and 2 as indicated in Figure 16. Figure 17 shows the water jet from the top of the structure impacting the flume bottom and spreading in all directions. The splash overtakes the modeled surge at the time of the snapshot and subsequently transforms into a surge traveling at a lower speed downstream. It reaches

gauge 2 at almost the same time as the modeled surge and falls behind the model results at gauge 3. Gauges 2 and 3 cannot be properly calibrated for the surge on a dry bottom therefore the recorded surface elevations do not represent the actual flow conditions for comparison with the model results.

Test 4 has two-thirds of the initial solitary wave height comparing to test 2 to investigate the nonlinear effects. Figure 18 shows improved agreement between the recorded and computed surface elevations downstream; however, the propagation speed discrepancy is still evident. The model also produces a better approximation of the surface elevation adjacent to the structure as seen in Figure 19. Overall, the model has better performance for smaller amplitude and longer waves supporting the use of the HLLS solver to model overtopping of tsunamis.

Test 5 has three quarters of the water depth of test 2 to increase the reflection from the front wall. As presented in Figure 20, gauge 1 recorded a distinct reflected peak from the wall that is slightly exaggerated by the model. The downstream gauges recorded a developing wave packet with increasing period. The model produces a solitary wave that match the recorded wave amplitude reasonably well. Figure 21 indicates good agreement of the recorded and computed surface profiles on the downstream side toward the end of the overtopping process. The model, however, overestimates the water on top of the structure due to leakage from the source term as illustrated in case 2 in Section 3.

The comparisons of the shallow-water model and the laboratory tests prove that the model can be implemented to provide adequate results when considering overtopping and wave formation on the downstream side of a defense structure.

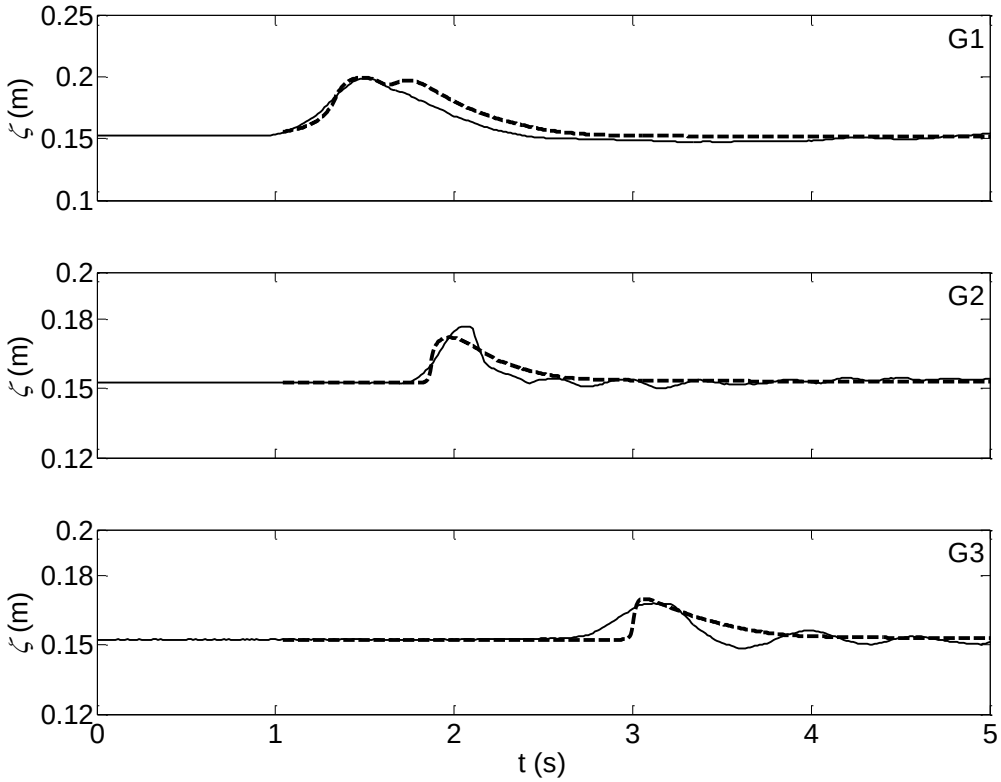

Figure 12: Time series of three gauges for test 1. Wave gauge shown as solid line, model results shown as dash line

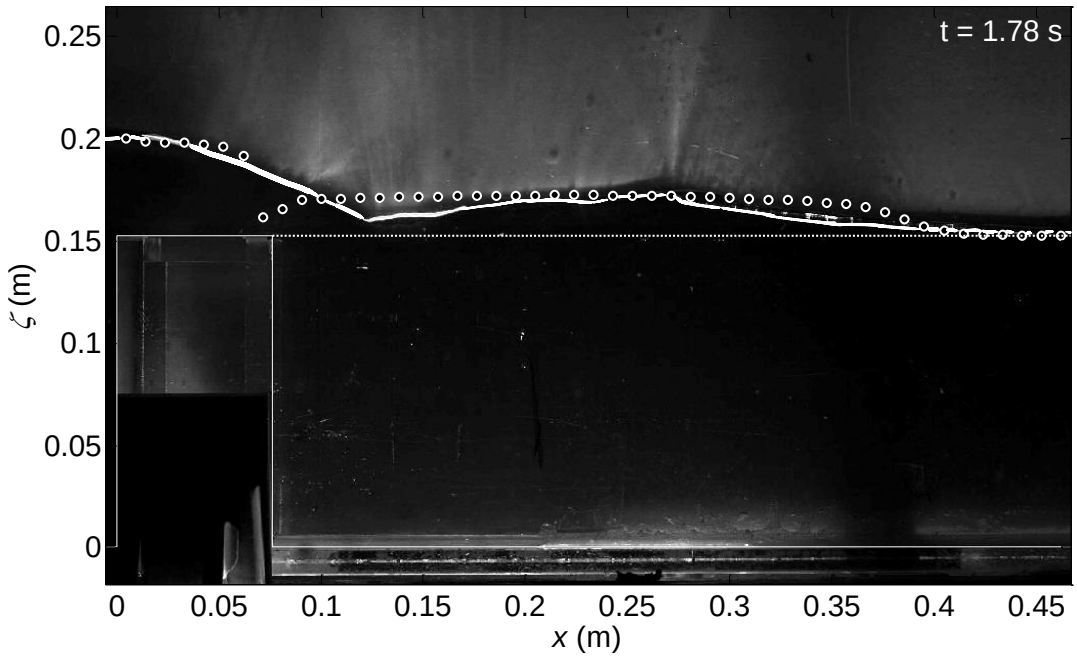

Figure 13: High-speed snapshot of test 1. Model results shown as white circle with black fill. Surface is highlighted by white line for ease of comparison.

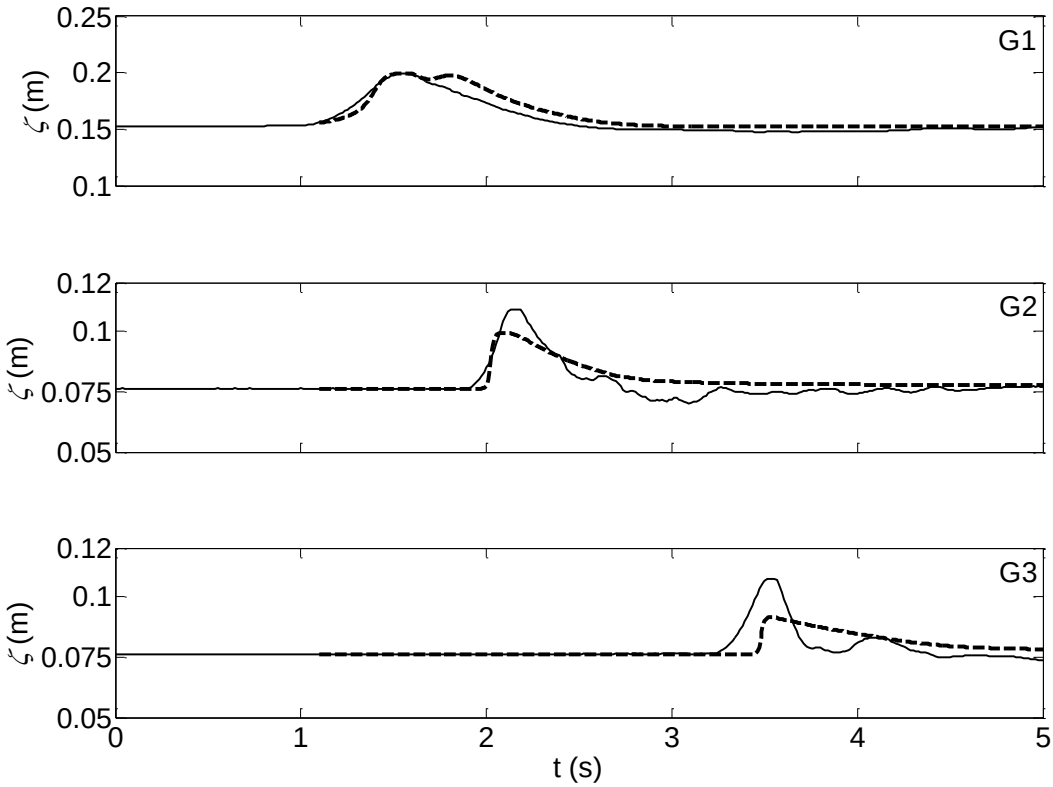

Figure 14: Time series of three gauges for test 2. Wave gauge shown as solid line, model results shown as dash line

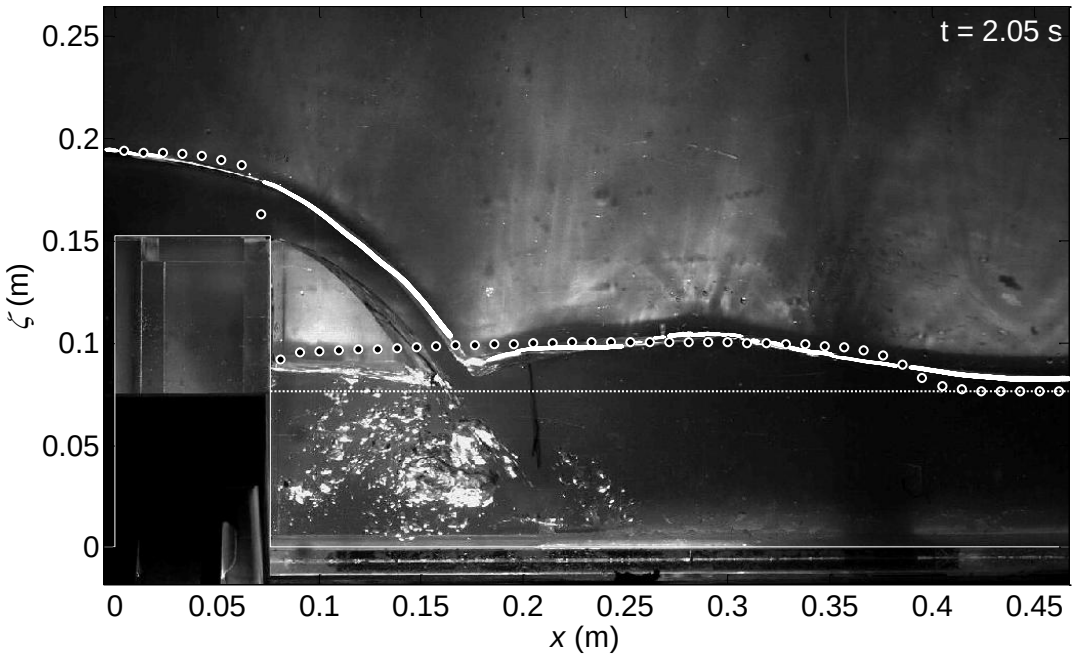

Figure 15: High-speed snapshot of test 2. Model results shown as white circle with black fill. Surface is highlighted by white line for ease of comparison.

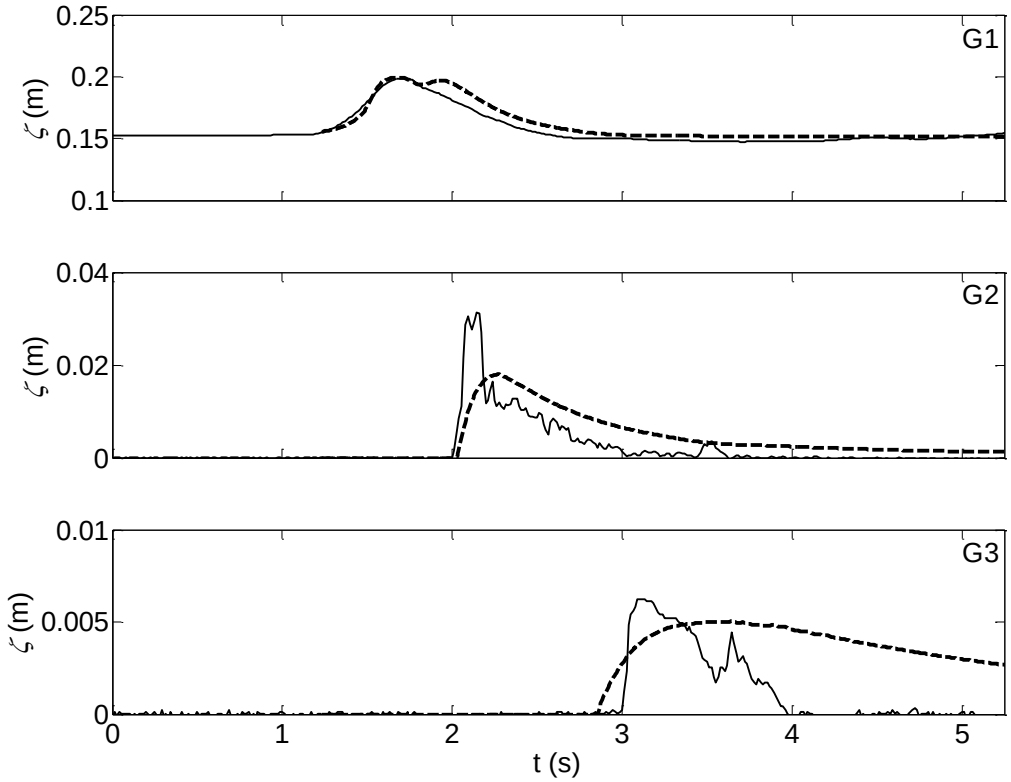

Figure 16: Time series of three gauges for test 3. Wave gauge shown as solid line, model results shown as dash line. Wave gauge does not show actual depth at gauge 2 and 3; only front arrival time.

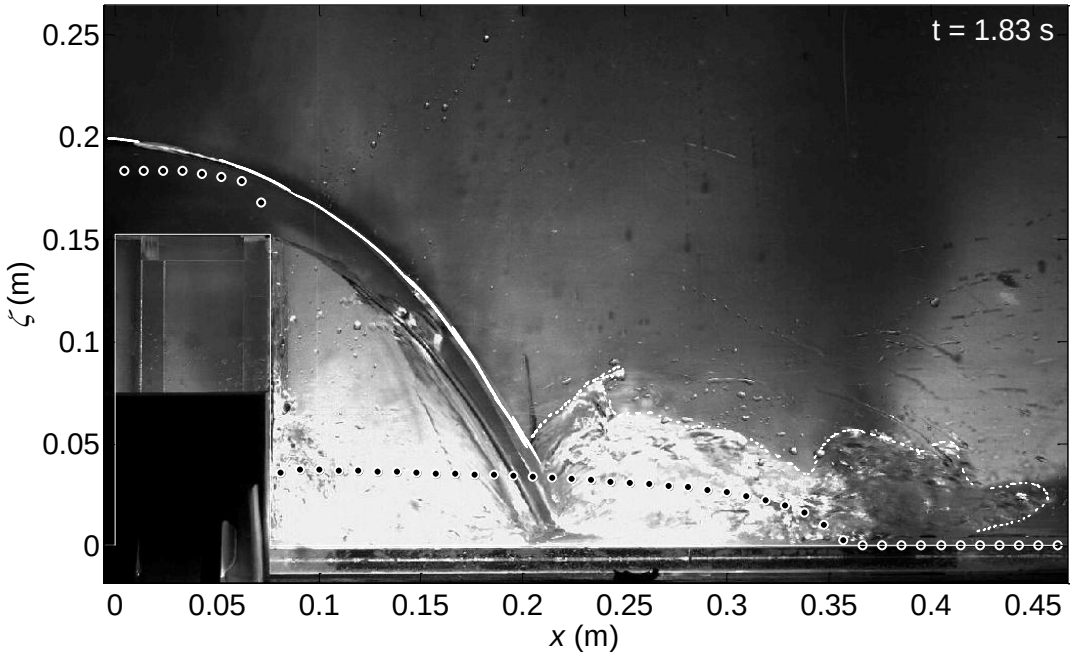

Figure 17: High-speed snapshot of test 3. Model results shown as white circle with black fill. Surface is highlighted by white line for ease of comparison.

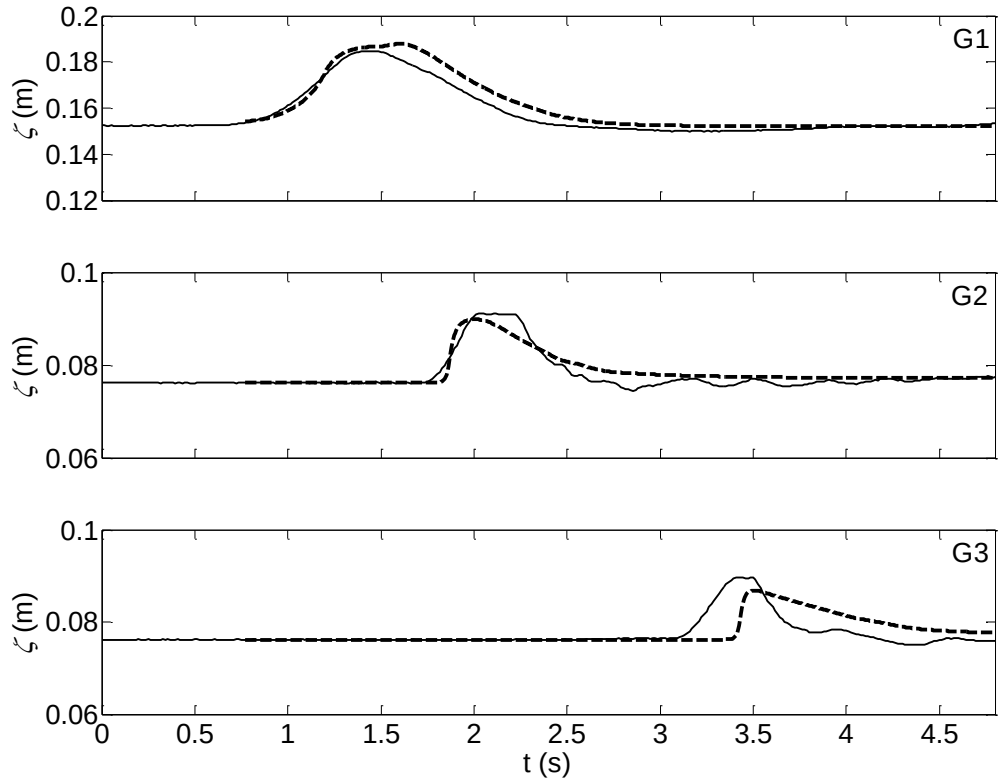

Figure 18: Time series of three gauges for test 4. Wave gauge shown as solid line, model results shown as dash line

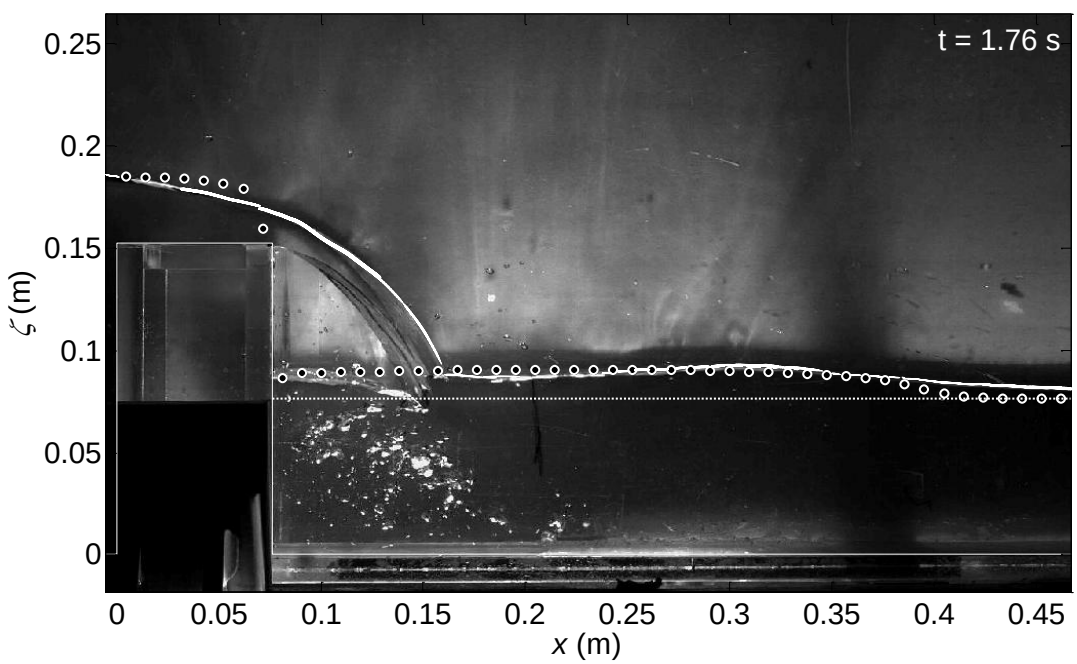

Figure 19: High-speed snapshot of test 4. Model results shown as white circle with black fill. Surface is highlighted by white line for ease of comparison.

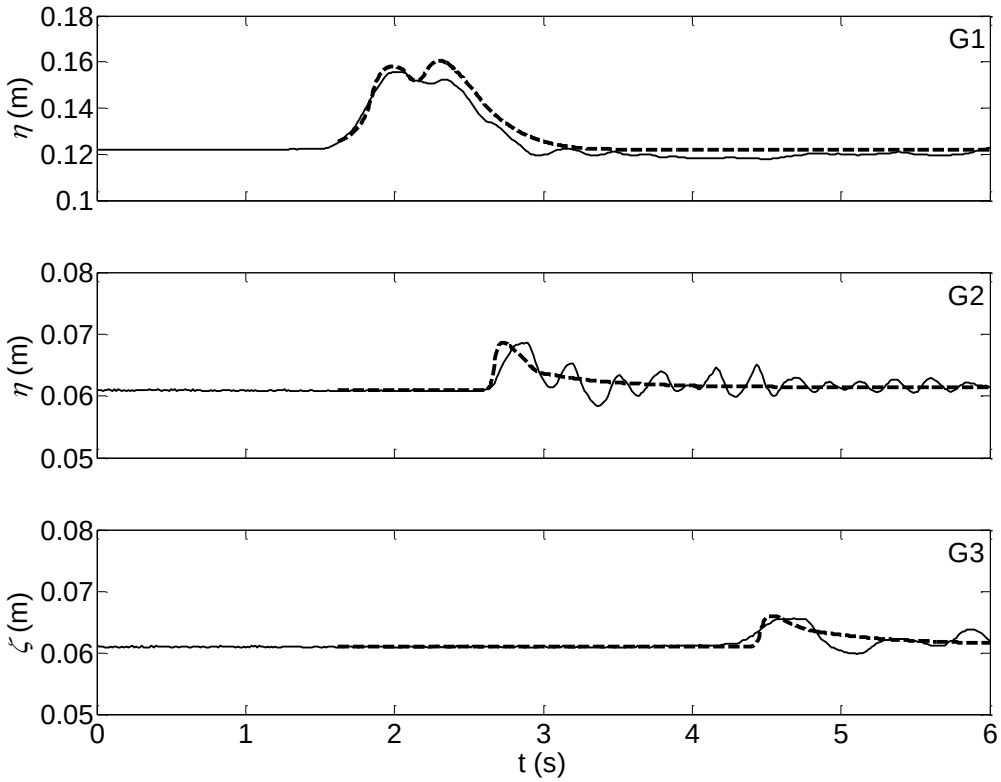

Figure 20: Time series of three gauges for test 5. Wave gauge shown as solid line, model results shown as dash line

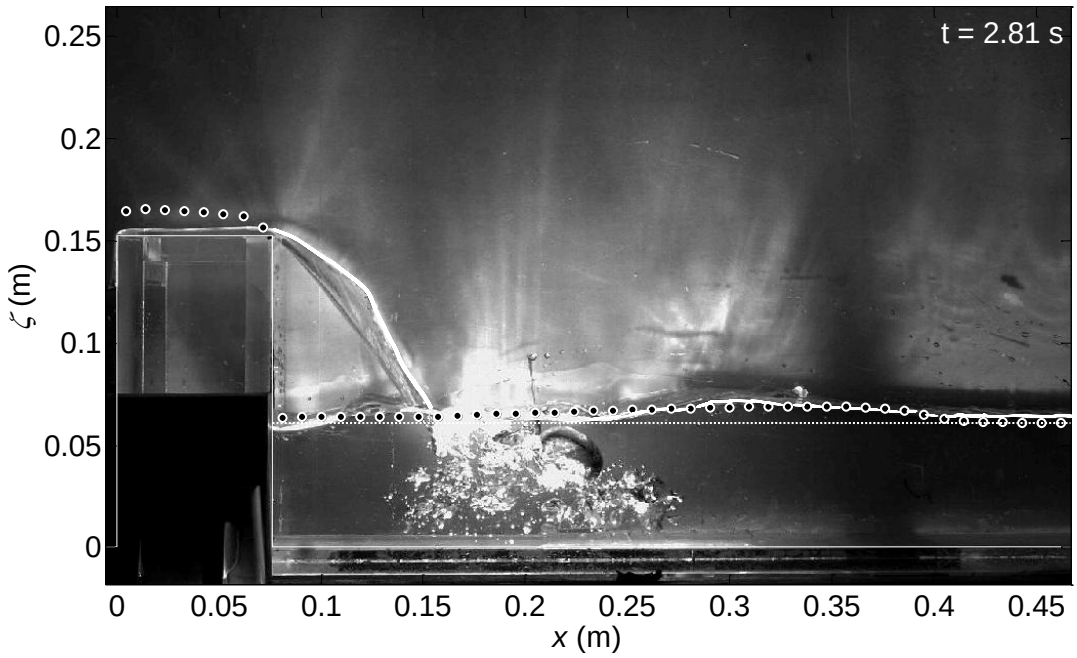

Figure 21: High-speed snapshot of test 5. Model results shown as white circle with black fill. Surface is highlighted by white line for ease of comparison.

5. Conclusions and Recommendations

The HLLS solver of the Riemann problem developed by Murillo and Garcia-Navarro (2010; 2012) provides a convenient tool to describe effects of overtopping on vertical breakwaters through a nonlinear shallow-water model. The solver includes a source term that can describe a vertical breakwater as bottom discontinuities and incorporates their effects on the flow momentum as hydrostatic forces. The multiphase solver of OpenFOAM and a specially-designed laboratory experiment provide results to assess the capability to model wave processes over bottom discontinuities and the downstream wave formation.

A series of test cases mimicking the Riemann problem allows examination of a shallow-water model with the HLLS solver in reproducing the basic flow features over a bottom discontinuity. Comparisons with OpenFOAM results show very good agreement for cases with zero initial velocity. The force acting on the bottom step deviates from the hydrostatic assumption as flow velocity increases, but still gives acceptable estimations of propagation speeds. For cases involving free fall of water, OpenFOAM produces a higher propagation speed due to air entrapped within the flow. Although the HLLS solver cannot describe the water fall, it provides a tool to approximate the fall effects.

The laboratory experiment allows evaluation of the HLLS solver for practical application with a vertical breakwater. Despite the simplicity of the formulation, the shallow-water model can provide a good qualitative description of the primary physical processes. These include downstream wave propagation as well as the partial wave reflection from the front face, the surge formation on the top, and the overtopping of the structure. The model, however, overestimates the reflected wave from the structure. This leads to an underestimation of the overtopping volume and the downstream wave height. As the wave propagates, the wave speed is underestimated due to processes that cannot be considered in the shallow-water model. The results improve with decreasing solitary wave amplitude, supporting the use of the HLLS solver

to model overtopping of tsunamis. This research only address the implementation of the HLLS solver in a nonlinear shallow-water model, but similar augmentation can be made to a non-hydrostatic or Boussinesq model to enhance the capability.

References

Allsop, N. W. H., Besley, P., Madurini, L., 1995. Overtopping performance of vertical walls and composite breakwaters, seawalls and low reflection alternatives. Final Report of Monolithic Coastal Structures Project, Univ. of Hannover, Hannover, Germany.

Bernetti, R., Titarev, V.A., Toro, E.F., 2008. Exact solution of the Riemann problem for the shallow water equations with discontinuous bottom geometry. *Journal of Computational Physics*, 227, 3212-3243.

Brady, P.D.M., Boutounet, M., Beecham, S., 2004. Free Surface Monitoring Using Image Processing. *Proceedings of 15th Australasian Fluid Mechanics Conference*, 13-17 December.

Bricker, J.D., Takagi, H., Mitsui, J., 2013. Turbulence model effects on VOF analysis of breakwater overtopping during the 2011 great east Japan tsunami. *IAHR World Congress*.

Bukreev, V.I., Gusev, A.V., Ostapenko, V.V., 2003. Breakdown of a discontinuity of the free fluid surface over a bottom step in a channel. *Fluid Dynamics*, 38, 889-899.

Einfeldt, B., 1988. On Godunov-type Methods for Gas Dynamics. *SIAM Journal of Numerical Analysis*, 25, 294-318.

Franco, L., de Gerloni, M., Van der Meer, J. W., 1994. Wave overtopping on vertical and composite breakwaters. Proceedings of 24th International Conference on Coastal Engineering, ASCE, Reston, VA, 1030-1045.

George, D.L., 2008. Augmented Riemann solvers for the shallow water equations over variable topography with steady states and inundation. *Journal of Computational Physics*, 227, 3089-3113.

Glaister, P., 1988. Approximate Riemann solutions of the shallow water equations. *Journal of Hydraulic Research*, 26, 293-306.

Godunov, S. K., 1959. A difference method for numerical calculation of discontinuous solutions of the equations of hydrodynamics. *Matematicheskii Sbornik*, 47, 271–306.

Hu, K., Mingham, C.G., Causon, D.M., 2000. Numerical simulations of wave overtopping of coastal structures using the non-linear shallow water equations. *Coastal Engineering*, 41, 433-465.

Liang, Q., Borthwick, A.G.L., 2009. Adaptive quadtree simulation of shallow flows with wet-dry fronts over complex topography. *Computers and Fluids*, 38, 221-234.

Lin, T.C., Hwang, K.S., Hsiao, S.C., and Yang, R.Y., 2012. An experimental observation of a solitary wave impingement, run-up and overtopping on a seawall. *Journal of Hydrodynamics*, 24(1), 76-85.

Mingham, C.G., Causon, D.M., 1998. High-resolution finite-volume method for shallow water flows. *Journal of Hydraulic Engineering*, 124, 605-614.

Murillo, J., Garcia-Navarro, P., 2010. Weak solutions for partial differential equations with source terms: Application to the shallow water equations. *Journal of Computational Physics*, 229, 4327-4368.

Murillo, J., Garcia-Navarro, P., 2012. Augmented versions of the HLL and HLLC Riemann solvers including source terms in one and two dimensions for shallow flow applications. *Journal of Computational Physics*, 231, 6861-6906.

Roe, P.L., 1981. Approximate Riemann solver, parameter vectors, and difference schemes. *Journal of Computational Physics*, 43, 357-372

Roeber, V., Cheung, K.F., 2012. Boussinesq-type model for energetic breaking waves in fringing reef environments. *Coastal Engineering*, 70, 1-20.

Sato, S., Okayasu, A., Yeh, H., Fritz, H. M., Tajima, Y., T. Shimozono, 2014. Delayed survey of the 2011 Tohoku tsunami in the former exclusion zone in Minami-Soma, Fukushima prefecture. *Pure Applied Geophysics*, 171, 3229-3240.

Shi, F., Kirby, J. T., Harris, J. C., Geiman, J. D., Grilli, S. T., 2012, A high-order adaptive time-stepping TVD solver for Boussinesq modeling of breaking waves and coastal inundation, *Ocean Modeling*, 43-44, 36-51.

Toro, E.F., 1992. Riemann problems and the WAF method for solving the two-dimensional shallow water equations. *Philosophical Transactions: Physical Sciences and Engineering*, 338, 43-68.

Toro, E.F., 1999. *Riemann Solvers and Numerical Methods for Fluid Dynamics: A Practical Introduction*. Berlin, Germany: Springer, 624p.

Van der Meer, J., Bruce, T., 2014. New physical insights and desing formulas on wave overtopping at sloping and vertical structures. *Journal of Waterway, Port, Coastal, Ocean Engineering*, 140, 04014025.

Wei, G., Kirby, J.T., 1995. A time-dependent numerical code for extended Boussinesq equations. *Journal of Waterway, Port, Coastal and Ocean Engineering*, 120, 251-261.

Weller, H.G., Tabor, G., Jasak, H., Fureby, C., 1998. A tonsorial approach to computational continuum mechanics using object oriented techniques. *Computers in Physics*, 12, 620-631.

Yim, S.C., Olsen, M.J., Cheung, K.F., Azadbakht, M., 2014. Tsunami modeling, fluid load simulation, and validation using geospatial field data. *Journal of Structural Engineering*, 140. A4014012.

Yoon, S.B., Lim, C.H., Choi, J., 2007. Dispersion-correction finite difference model for simulation of transoceanic tsunamis. *Terrestrial, Atmospheric and Oceanic Sciences.*, 18, 31-53.

Zhou, J.G., Causon, D.M., Ingram, D.M., Mingham, C.G., 2002. Numerical solutions of the shallow water equations with discontinuous bed topography. *International Journal for Numerical Methods in Fluids*, 38, 769-788.

Zhou, J.G., Causon, D.M., Ingram, D.M., Mingham, C.G., 2001. The surface gradient method for the treatment of source terms in the shallow-water equations. *Journal of Computational Physics*, 168, 1-25.